

EzGal: A Flexible Interface for Stellar Population Synthesis Models

CONOR L. MANCONE AND ANTHONY H. GONZALEZ

Department of Astronomy, University of Florida, Gainesville, FL 32611; cmancone@astro.ufl.edu,
anthony@astro.ufl.edu

Received 2011 July 26; accepted 2012 April 26; published 2012 June 1

ABSTRACT. We present EzGal, a flexible Python program designed to easily generate observable parameters (magnitudes, colors, and mass-to-light ratios) for arbitrary input stellar population synthesis (SPS) models. As has been demonstrated by various authors, for many applications the choice of input SPS models can be a significant source of systematic uncertainty. A key strength of EzGal is that it enables simple, direct comparison of different model sets so that the uncertainty introduced by choice of model set can be quantified. Its ability to work with new models will allow EzGal to remain useful as SPS modeling evolves to keep up with the latest research (such as varying IMFs). EzGal is also capable of generating composite stellar population models (CSPs) for arbitrary input star-formation histories and reddening laws, and it can be used to interpolate between metallicities for a given model set. To facilitate use, we have created an online interface to run EzGal and quickly generate magnitude and mass-to-light ratio predictions for a variety of star-formation histories and model sets. We make many commonly used SPS models available from the online interface, including the canonical Bruzual & Charlot models, an updated version of these models, the Maraston models, the BaSTI models, and the Flexible Stellar Population Synthesis (FSPS) models. We use EzGal to compare magnitude predictions for the model sets as a function of wavelength, age, metallicity, and star-formation history. From this comparison we quickly recover the well-known result that the models agree best in the optical for old solar-metallicity models, with differences at the ~ 0.1 mag level. Similarly, the most problematic regime for SPS modeling is for young ages ($\lesssim 2$ Gyr) and long wavelengths ($\lambda \gtrsim 7500$ Å), where thermally pulsating AGB stars are important and scatter between models can vary from 0.3 mag (Sloan i) to 0.7 mag (K_s). We find that these differences are not caused by one discrepant model set and should therefore be interpreted as general uncertainties in SPS modeling. Finally, we connect our results to a more physically motivated example by generating CSPs with a star-formation history matching the global star-formation history of the universe. We demonstrate that the wavelength and age dependence of SPS model uncertainty translates into a redshift-dependent model uncertainty, highlighting the importance of a quantitative understanding of model differences when comparing observations with models as a function of redshift.

Online material: color figures

1. INTRODUCTION

Stellar population synthesis (SPS) modeling provides a valuable tool for studying the evolution of a stellar population as a function of time. For this reason, there have been multiple efforts to develop software for modeling the evolution of the spectral energy distribution (SED) of a stellar population. Because there are a number of unknowns in SPS modeling, such as details of post-main-sequence stellar evolution and the form of the initial mass function, models from different groups yield a range of results, due to different input ingredients in their models. A detailed discussion of these uncertainties and their impact can be found in Conroy et al. (2009, hereafter C09) and Conroy & Gunn (2010). The net result is that the choice of model set is itself a source of uncertainty when using SPS models.

The use of SPS models is a central ingredient for a wide range of active research programs, as is evident from a simple

literature search. SPS models are commonly used to perform SED fitting and to estimate a diverse set of properties for stellar populations, including ages, redshifts, k -corrections, and masses (see, for example, Blanton & Roweis 2007; Taylor et al. 2011; Ma et al. 2012; Fotopoulou et al. 2012). They are used to fit isochrones to color-magnitude diagrams, to measure ages and metallicities of resolved stellar populations, to measure the strength of spectral features in observed galaxies, to predict the evolution of a stellar population as a function of age, and to predict observables from simulations (for example, Jonsson 2006; Marín-Franch et al. 2009; Mancone et al. 2010; Kriek et al. 2011). Because of the utility and ubiquity of SPS models, it is important to have simplifying methods for comparing the models with observations, as well as with each other.

Of the many SPS model sets, the most commonly used is that of Bruzual & Charlot (2003, hereafter BC03), which we use as

a reference for comparisons because of its wide use. Another commonly used model set is that of Maraston (2005, hereafter M05), which includes a detailed treatment of thermally pulsating asymptotic giant branch (TP-AGB) stars, which can dominate the infrared light of a young stellar population. An updated treatment of the TP-AGB phase is also incorporated into the latest version of the BC03 models (Charlot & Bruzual 2007, private communication, hereafter CB07). More recent work includes the BaSTI models from Percival et al. (2009, hereafter P09), which includes not only a range of metallicities, but also α -enhanced models. The FSPS models from C09 and Conroy & Gunn (2010) are unique in their ability to treat the most important SPS inputs (such as initial mass function [IMF] or various uncertain phases of stellar evolution) as free parameters, allowing the uncertainties introduced by various SPS inputs to be quantitatively measured.

All of these models predict the evolution of the SED of a stellar population as a function of age, given a star-formation history, IMF, and metallicity. However, the easiest-to-measure observables are not the SED or age, but the magnitude and redshift. Therefore, all of these model sets are most useful when they can be easily translated into predictions of magnitude evolution as a function of redshift. This transformation involves assuming a formation redshift (the redshift at which star formation starts), calculating a cosmology-dependent luminosity distance, and projecting the SEDs through filter response curves to calculate magnitudes, e -corrections, and k -corrections. The e -corrections specify the amount of observed magnitude evolution that is due to the aging of a stellar population, while the k -corrections specify the amount of evolution due to observing a different part of the SED at different redshifts. Together, the e -corrections, k -corrections, and distance moduli specify the magnitude evolution of a stellar population as a function of redshift.

While these steps are straightforward, in the past there has not been a simple and consistent tool to do this for all model sets. BC03 and C09 both come with code for calculating magnitude evolution as a function of redshift, and both come with a number of commonly used filter response curves for user convenience. In contrast, P09 and M05 calculate and distribute the absolute magnitude evolution of the stellar populations for a fixed set of filters.

This lack of directly comparable outputs between different model sets is the reason that we have developed EzGal, a Python program that calculates magnitude evolution as a function of redshift from models of the evolution of an SED as a function of age. EzGal comes with a number of the most commonly used filter response curves, and more can be easily added by the user. It includes the latest Vega spectrum from the Space Telescope Science Institute (STScI)¹ so that magnitudes can be calculated on both the Vega and AB systems. By using the stellar mass

information that comes with all of these model sets, EzGal can also calculate mass-to-light ratios in any filter. This requires calculating the absolute magnitude of the Sun in any filter, and so the latest solar spectrum from STScI² is also included with EzGal. EzGal can interpolate between models, which is useful for generating models with the same metallicity from different model sets. It can also generate CSPs with arbitrary input star-formation histories or dust-reddening laws. Finally, EzGal can read in SEDs in ASCII format or in the binary `isecd` format in which the BC03 and CB07 models are distributed. In principle, this allows it to work with any model, enabling easy comparison with any new codes in the future. EzGal is designed to be an easy-to-use tool for predicting observables from SPS models and greatly simplifying the task of comparing different SPS model sets.

This article explains how EzGal works and gives a detailed comparison between commonly used model sets. Section 2 describes details of how EzGal works and discusses calculating magnitudes (§ 2.1), generating composite stellar populations (§ 2.2), and calculating masses and mass-to-light ratios (§ 2.3). In § 3 we present a detailed comparison between the model sets. Section 4 lists EzGal resources currently available from the Internet, such as the World Wide Web interface. Our conclusions are found in § 5.

2. PROGRAM PROCEDURE

2.1. Calculating Magnitudes

EzGal calculates apparent magnitudes, absolute magnitudes, e -corrections, and k -corrections from the model sets as a function of redshift. Conceptually, these quantities are all easy to calculate and are derived from the rest-frame and observed-frame absolute magnitudes as a function of age and redshift. EzGal uses equation (1) to calculate observed-frame absolute magnitudes as a function of redshift (z) and formation redshift (z_f):

$$\begin{aligned}
 M_{AB}[z, t(z, z_f)] & \\
 &= -2.5 \log \left[\frac{\int_{-\infty}^{\infty} \nu^{-1} (1+z) F_{\nu}[\nu(1+z), t(z, z_f)] R(\nu) d\nu}{\int_{-\infty}^{\infty} \nu^{-1} R(\nu) d\nu} \right] \\
 &\quad - 48.60.
 \end{aligned}
 \tag{1}$$

This equation calculates the absolute AB magnitude as a function of redshift and age, $M_{AB}[z, t(z, z_f)]$, for an SPS model by projecting the redshifted SED, $F_{\nu}[\nu(1+z), t(z, z_f)]$, at the given age, $t(z, z_f)$ (with the age determined by redshift and formation redshift), through the filter response curve, $R(\nu)$, and comparing this with the flux of a 0 mag AB source. For the purposes of this equation, the SED should have units of

¹ See <http://www.stsci.edu/hst/observatory/cdbs/calspec.html>.

² See http://documents.stsci.edu/hst/wfpc2/documents/handbooks/cycle17/ch6_exposuretime2.html#480221.

ergs⁻¹ Hz⁻¹ cm⁻² and should be the observed flux for a galaxy at a distance of 10 pc. The age of the galaxy, $t(z, z_f)$, is given by $t(z, z_f) = T_U(z) - T_U(z_f)$, where $T_U(z)$ is the age of the universe as a function of redshift, given the cosmology. By default, EzGal assumes a WMAP7 cosmology (Komatsu et al. 2011; $\Omega_m = 0.272$, $\Omega_\Lambda = 0.728$, and $h = 0.704$), although any cosmology can be used. To calculate the rest-frame absolute magnitude, EzGal calculates $M_{AB}[0, t(z, z_f)]$.

EzGal also calculates a number of filter properties using standard STScI definitions, including mean wavelength, pivot wavelength, average wavelength, effective dimensionless Gaussian width, effective width, equivalent width, and rectangular width.^{3,4} The conversion from AB to Vega magnitudes is calculated for each filter by using the included Vega spectrum to calculate the AB magnitude of Vega in the filter. The Vega spectrum is described in Bohlin & Gilliland (2004) and comes from IUE spectrophotometry from 0.12–0.17 μm , *Hubble Space Telescope (HST)* Space Telescope Imaging Spectrograph from 0.17–1.01 μm , and a Kurucz model atmosphere at longer wavelengths. Finally, the absolute magnitude of the Sun is also calculated by projecting the solar spectrum through the filter response curve in the same way as everything else. The solar spectrum used by EzGal is an observed spectrum of the Sun from 0.12–2.5 μm (Colina et al. 1996), which we have extended using a Kurucz model atmosphere at longer wavelengths. Specifically, we take a model atmosphere with solar metallicity, $T_{\text{eff}} = 5777$ K, and $\log_g = 4.44$; normalize it to match the observed solar spectrum from 1.5–2.5 μm ; and then use it where the observed spectrum ends.

2.2. Calculating Composite Stellar Populations

EzGal generates CSP models from simple stellar population (SSP) models in the standard way. Conceptually, the SED of a CSP at some age is given by a weighted average of SSPs as a function of age, where the weight for a given SSP is equal to the relative strength of star formation (compared with the total amount of star formation) for the CSP at that time. The effect of dust can also be included if desired. Mathematically, EzGal uses equation (2) to calculate the evolution of the SED of a CSP as a function of time:

$$F(\lambda, t) = \frac{\int_0^t \Psi(t-t') F_{\text{SSP}}(\lambda, t') \Gamma(\lambda, t') dt'}{\int_0^{T_U} \Psi(t') dt'}. \quad (2)$$

In this equation $F(\lambda, t)$ is the flux of the CSP as a function of wavelength and time, $\Psi(t)$ is the star-formation rate as a function of time, $F_{\text{SSP}}(\lambda, t')$ is the flux of the SSP as a function of

wavelength and time, $\Gamma(\lambda, t')$ is the impact of dust as a function of wavelength and time, and T_U is the age of the universe at $z = 0$. The factor of $\int_0^{T_U} \Psi(t') dt'$ normalizes the CSP such that one solar mass of stars is generated over the entire star-forming epoch. EzGal can work with arbitrary star-formation histories and dust laws. A typical dust law is a Charlot & Fall (2000) dust law with $\Gamma(\lambda) = e^{-\tau(t)(\lambda/5500 \text{ \AA})^{-0.7}}$, where $\tau(t) = 1.0$ for $t \leq 10^7$ yr and $\tau(t) = 0.5$ for $t > 10^7$ yr. Equation (2) represents the same general methodology used by BC03 and C09 to generate CSPs. M05 uses a different normalization and instead divides by $\int_0^t \Psi(t') dt'$ so that the CSPs have one solar mass of stars at all ages. P09 does not provide any CSPs with its models.

In practice, EzGal uses Simpson's rule to numerically evaluate the top integral in equation (2). When performing numeric integration, it is often necessary to subsample the age grid of the SSPs to properly sample any sharp features in the star-formation history or in the evolution of the SEDs. In order to minimize execution time and still ensure high fidelity in the numeric integration, EzGal uses an iterative algorithm to decide how finely to subsample the age grid. EzGal performs the integral in equation (2) at wavelengths of 3000, 8000, and 12000 \AA with increasingly finer levels of age subsampling until the difference between two subsequent integrals drops below some tunable threshold (in magnitude).

We verify our procedure for generating CSPs by comparing magnitude predictions for CSPs generated with EzGal from BC03 and C09 models with magnitude predictions for CSPs generated by the code distributed with BC03 and C09. We find differences that are small and negligible: for BC03 the differences in magnitude are less than 0.005 mag for short ($\tau = 0.1$ Gyr) and long ($\tau = 1.0$ Gyr) dust-free exponentially decaying bursts, and for C09 the differences are less than 0.01 mag for short bursts and less than 0.005 mag for long bursts. These differences are larger than the maximum error set in our numerical integration (0.001 mag), but errors at these levels can easily be accounted for by small differences in the procedures used by different groups.

2.3. Calculating Mass-to-Light Ratios and Masses

To calculate rest-frame mass-to-light ratios in any filter, F , given redshift and formation redshift, four pieces of information are required: the age as a function of redshift and formation redshift, $t(z, z_f)$; the stellar mass as a function of age, $M_*(t(z, z_f))$; the rest-frame absolute magnitude of the stellar population as a function of age, $M_F[t(z, z_f)]$; and the absolute magnitude of the Sun in the filter, $M_{\odot, F}$. Again, the conversion from redshift and formation redshift to age requires assuming a cosmology, for which EzGal defaults to a WMAP7 cosmology (Komatsu et al. 2011; $\Omega_m = 0.272$, $\Omega_\Lambda = 0.728$, and $h = 0.704$). The rest-frame mass-to-light ratio in a given filter as a function of redshift

³ See http://www.stsci.edu/hst/wfpc2/documents/handbook/cycle17/ch6_exposuretime2.html#480221.

⁴ See http://www.stsci.edu/hst/wfc3/documents/handbooks/currentIHB/c06_uvvis06.html#57.

and formation redshift is then given by

$$\frac{M_*}{L_F}(z, z_f) = \frac{M_*[t(z, z_f)]}{10^{-0.4\{M_F[t(z, z_f)] - M_{\odot,F}\}}}. \quad (3)$$

EzGal uses equation (3) to calculate rest-frame mass-to-light ratios. It uses its own calculation of the absolute magnitude evolution of a stellar population as a function of age, calculates the absolute magnitude of the Sun using the solar spectrum from STScI, and gets stellar masses directly from the model sets (which typically distribute stellar mass as a function of age, along with the SED). The resulting mass-to-light ratios depend on the chosen model set, star-formation history, and initial mass function. EzGal also calculates an observed-frame mass-to-light ratio as a function of redshift using the observed-frame absolute magnitude of the model and the observed-frame absolute magnitude of the Sun. The latter is calculated by redshifting the solar spectrum to the given redshift and projecting it through the bandpass normally.

For the purposes of estimating the mass of an observed galaxy, only two pieces of information are required from the models: the stellar mass as a function of redshift and the apparent magnitude of the model as a function of redshift. With these values determined, the mass of an observed galaxy with an assumed redshift (z) and formation redshift (z_f) can be calculated as

$$M_{*,g}(z, z_f) = M_*(z, z_f) * 10^{-0.4(m_{g,F} - m_F(z, z_f))}, \quad (4)$$

where $M_*(z, z_f)$ is the stellar mass of the model as a function of z and z_f , $m_{g,F}$ is the apparent magnitude of the galaxy in a given passband, and $m_F(z, z_f)$ is the apparent magnitude of the model in the same passband as a function of z and z_f .

3. MODEL COMPARISON

3.1. Model-Set Overview

In this article we compare results from five different SPS model sets: BC03, M05, CB07, P09, and C09. These model sets include a varying range of metallicities and IMFs, and they have different spectral resolutions and age grids. M05 has the highest-metallicity model ($Z = 3.5 Z_{\odot}$), while BC03, CB07, and P09 have the lowest ($Z = Z_{\odot}/200$). C09 has the

finest grid in metallicity space, with 22 metallicities from $Z = 0.01 Z_{\odot} - 1.5 Z_{\odot}$, and is the only model set that distributes models with all three common IMFs: Salpeter, Chabrier, and Kroupa. Finally, P09 is the only model set herein to publish models with α -enhanced metallicities. This information is provided as a quick reference for comparing model sets and is summarized in Table 1, which includes the number of ages in each model set, the number of metallicities provided, and the IMFs provided.

To facilitate direct comparisons between model sets, we interpolate between the models to generate a new set of models for each model set with the same metallicities. Our new models have metallicities of $Z = 0.05, 0.1, 0.2, 0.4, 0.8, 1.0,$ and 1.5 times Z_{\odot} or $Z = 0.001, 0.002, 0.004, 0.008, 0.016, 0.02,$ and 0.03 . For all of our following comparisons, we use these interpolated models. We also choose to restrict our comparisons to models with the same IMF. As there is no IMF that is covered by all five model sets we do all comparisons using a Salpeter IMF; therefore, in the following comparisons, the models from P09 are not included. For each of our interpolated models, we use EzGal to generate four CSP models. The CSPs are dust-free, exponentially decaying bursts with e -folding timescales of 0.1, 0.5, 1.0, and 10.0 Gyr.

3.2. Filter-Set Overview

For convenience to EzGal users and to enable a basic model comparison, we generate a filter set for use with EzGal. Our filter set includes many commonly used filters: the Galaxy Evolution Explorer (*GALEX*) far-ultraviolet (FUV) and near-ultraviolet (NUV) filters, the Sloan filters, all wide *HST* Advanced Camera for Surveys (ACS) Wide Field Channel (WFC) and Wide Field Camera 3 (WFC3) filters, Two Micron All Sky Survey (2MASS) filters, *Spitzer* Infrared Array Camera (IRAC) filters, and the Wide-field Infrared Survey Explorer (WISE) 3.4 and 4.6 μm filters. The filters come from a number of sources and all represent total transmission: CCD, telescope, filter, and a basic atmosphere when appropriate. The properties of the filter set are summarized in Table 2, which has the pivot wavelength and rectangular width for each filter, as well as the absolute AB magnitude of the Sun through each filter and the calculated AB-to-Vega conversion. The latter is in magnitudes, such that the Vega magnitude of a galaxy is its AB magnitude plus the listed conversion. The table is also reproduced on the Web for quick reference.

TABLE 1
MODEL-SET PROPERTIES

Name	No. ages	Metallicity (Z/Z_{\odot})	α -enhanced	No. metallicities	Salpeter	Chabrier	Kroupa
BC03	221	0.005-2.5	No	6	Yes	Yes	No
M05	68	0.05-3.5	No	5	Yes	No	Yes
CB07	221	0.005-2.5	No	6	Yes	Yes	No
P09	56	0.005-2	Yes	10	No	No	Yes
C09	189	0.01-1.5	No	22	Yes	Yes	Yes

TABLE 2
FILTER DATA

Name	Pivot wavelength (Å)	Rectangular width (Å)	M_{\odot} (AB)	Vega-AB
<i>GALEX</i> far-UV	1536	246	17.20	-2.093
<i>GALEX</i> near-UV	2300	730	10.04	-1.659
Sloan <i>u</i>	3556	558	6.37	-0.916
ACS WFC F435W	4318	845	5.37	0.102
WFC3 F438W	4325	616	5.34	0.152
Sloan <i>g</i>	4702	1158	5.12	0.100
ACS WFC F475W	4746	1359	5.10	0.096
WFC3 F475W	4773	1343	5.08	0.096
WFC3 F555W	5308	1563	4.86	0.023
ACS WFC F555W	5360	1124	4.84	0.005
WFC3 F606W	5887	2183	4.73	-0.085
ACS WFC F606W	5921	1992	4.72	-0.088
Sloan <i>r</i>	6175	1111	4.64	-0.144
WFC3 F625W	6241	1461	4.64	-0.150
ACS WFC F625W	6311	1308	4.63	-0.165
Sloan <i>i</i>	7489	1045	4.53	-0.357
WFC3 F775W	7647	1170	4.53	-0.382
ACS WFC F775W	7691	1320	4.53	-0.389
WFC3 F814W	8026	1538	4.52	-0.419
ACS WFC F814W	8055	1733	4.52	-0.425
Sloan <i>z</i>	8946	1125	4.51	-0.518
ACS WFC F850lp	9013	1239	4.51	-0.521
WFC3 F850lp	9167	1181	4.52	-0.522
WFC3 F105W	10550	2649	4.53	-0.647
WFC3 F110W	11534	4430	4.54	-0.761
<i>J</i>	12469	2088	4.56	-0.901
WFC3 F125W	12486	2845	4.56	-0.903
WFC3 F140W	13922	3840	4.60	-1.078
WFC3 F160W	15370	2683	4.65	-1.254
<i>H</i>	16448	2538	4.70	-1.365
K_s	21623	2642	5.13	-1.838
WISE 3.4 μm	33682	6824	5.95	-2.668
IRAC 3.6 μm	35569	6844	6.07	-2.787
IRAC 4.5 μm	45020	8707	6.57	-3.260
WISE 3.6 μm	46179	10508	6.62	-3.307
IRAC 5.8 μm	57450	12441	7.05	-3.753
IRAC 8 μm	79156	25592	7.67	-4.394

NOTE.—An up-to-date copy of this table is reproduced at <http://www.baryons.org/ezgal/filters.php>.

3.3. Comparison

We begin our comparison by examining the fidelity of magnitude predictions for the models in Sloan filters. Figure 1 shows the predicted *i*-band rest-frame absolute magnitude (*top*) and *g* – *i* color as a function of age for SSP models with a solar metallicity and Salpeter IMF. As can be seen from this figure, differences are typically ~ 0.1 – 0.2 mag. To better explore how the scatter depends on age and wavelength, we plot the scatter between models as a function of age, wavelength, metallicity, and star-formation history in Figure 2. The top left panel of this figure illustrates the scatter between the predicted magnitudes of the models (BC03, M05, CB07, and C09) for the Sloan filters *u*, *g*, *r*, *i*, and *z* as a function of age for an SSP with a Salpeter IMF and a metallicity of $Z = 0.001$. The

panels to the right show the same thing, but for $Z = 0.008, 0.02$, and 0.03 . The bottom row of panels shows the impact of changing star-formation histories. All the models in the bottom panel have solar metallicity ($Z = 0.02$) and a Salpeter IMF. The first plot on the bottom row shows the figure legend. The second plot shows the scatter between the model sets for an SSP, the next is for a dust-free exponentially decaying burst of star formation with an *e*-folding time (τ) of 1.0 Gyr, and the last is for a dust-free exponential burst with $\tau = 10.0$ Gyr. Scatter in this case refers to the standard deviation of the magnitudes predicted by the different models at a given age and through a particular filter.

A number of conclusions can be drawn from Figure 2. First, the best-case comparison is for solar metallicities and intermediate-to-old ages ($\gtrsim 4$ Gyr), for which differences between the models are

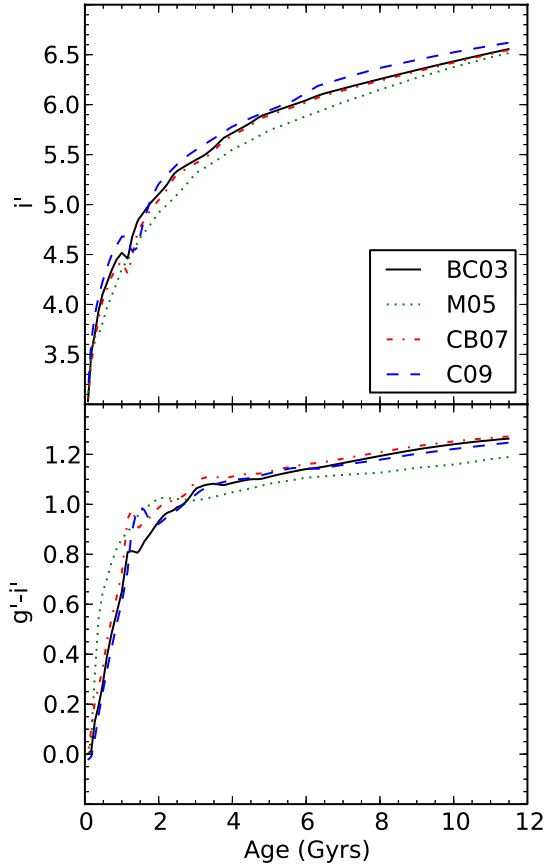


FIG. 1.—Comparison between the predicted i -band rest-frame absolute magnitudes (top) and $g - i$ colors (bottom) as a function of age for solar-metallicity SSPs with a Salpeter IMF. Magnitudes and colors are on the AB system. See the electronic edition of the *PASP* for a color version of this figure

(at most) 0.1 mag and drop to ~ 0.05 mag at the oldest ages. For the Sloan i and Sloan z filters, the scatter increases by a factor of ~ 2 for younger ages ($\lesssim 2$ Gyr). This is particularly true for subsolar metallicities, and the scatter in Sloan i and Sloan z increases systematically at these young ages when going from metallicities of $Z = 0.02$ to $Z = 0.008$ and 0.001 , reaching differences as large as ~ 0.4 mag. For the three bluest Sloan filters, the scatter is $\lesssim 0.1$ mag for all ages and metallicities.

The bottom series of panels in Figure 2 highlights the impact of an extended star-formation history, the effect of which is to smooth out the scatter between models as a function of age. At longer wavelengths, when the models differ more at younger ages, this smoothing has a tendency to increase errors at latter times and to decrease errors at earlier times. Therefore, in this case, model uncertainty for extended star-formation histories will be larger at later times if the star-formation history includes a substantial presence of young stars (ages $\lesssim 3$ Gyr).

Figure 3 is the same as Figure 2, but now various near-IR bands are plotted: J , H , and K_s and *Spitzer*/IRAC 3.6 and

4.5 μm . The first thing to note is that for an older ($\gtrsim 3$ Gyr) solar-metallicity SSP, the differences in JHK_s are comparable with the differences in the Sloan bands (i.e., Fig. 2), while the *Spitzer*/IRAC bands typically have larger errors in this same regime. The scatter between the models now has a stronger age dependency, and for ages $\lesssim 2$ Gyr the model uncertainty increases to 0.3 mag (J) and 0.6 mag (3.6 μm). Metallicity has the opposite impact on the scatter between models in the NIR for young ($\lesssim 3$ Gyr) and intermediate-to-old ($\gtrsim 3$ Gyr) stellar populations. For younger ages the scatter increases systematically while going to lower metallicities. This effect is particularly pronounced in the K_s band, which has a maximum scatter of ~ 0.35 mag for young stellar populations with solar metallicity, but a maximum scatter of ~ 0.7 mag for young stellar populations with $Z = 0.001$. For older stellar populations, the scatter is roughly constant or even decreases (IRAC 3.6 and 4.5 μm) as the metallicity decreases.

The general trend of increasing scatter toward younger ages is not a new discovery, but it is strongly influenced by uncertainties with the TP-AGB phase (M05; Marigo et al. 2008; C09). This short-lived phase in stellar evolution is poorly understood observationally, due to its rarity, and theoretically, because the properties of a TP-AGB star are strongly dependent upon mass loss, which is not predicted theoretically (Conroy et al. 2009). Unfortunately, for stellar modeling, TP-AGB stars can dominate the light of a stellar population at long wavelengths ($\lambda \gtrsim 1 \mu\text{m}$) for ages $\gtrsim 10^8$ yr. While it is most important in the NIR, it can also impact red optical filters to a smaller extent (C09), and so it can readily explain the systematic trend to higher scatters seen as a function of wavelength and age in Figures 2 and 3. Moreover, it can exacerbate differences for models with different metallicities, because the TP-AGB stars used to calibrate the models typically have unknown metallicities (Conroy et al. 2009), creating an additional source of uncertainty. This likely explains the substantially higher scatter seen for young ages, subsolar metallicities, and long wavelengths.

The differences seen in Figures 2 and 3 are best viewed as lower limits for the uncertainties introduced by SPS modeling. This is because agreement between the models can simply be caused by similar methodologies used by the various modeling groups and does not necessarily imply that the models are doing a better job of agreeing with actual stellar populations. For instance, we noted above that for old stellar populations the scatter between models for subsolar metallicities is typically the same as, or smaller than, the scatter for solar metallicities. This fact is not surprising, since all the model sets used herein are all compared with (or calibrated to match) Milky Way globular clusters, which are old and metal-poor systems.

Figure 4 demonstrates that the scatters seen in Figures 2 and 3 are not driven by just one model set. This figure shows the differences between the predicted magnitudes of these four models through the Sloan and NIR filters for four different ages and two metallicities. All the models in this figure are SSPs with

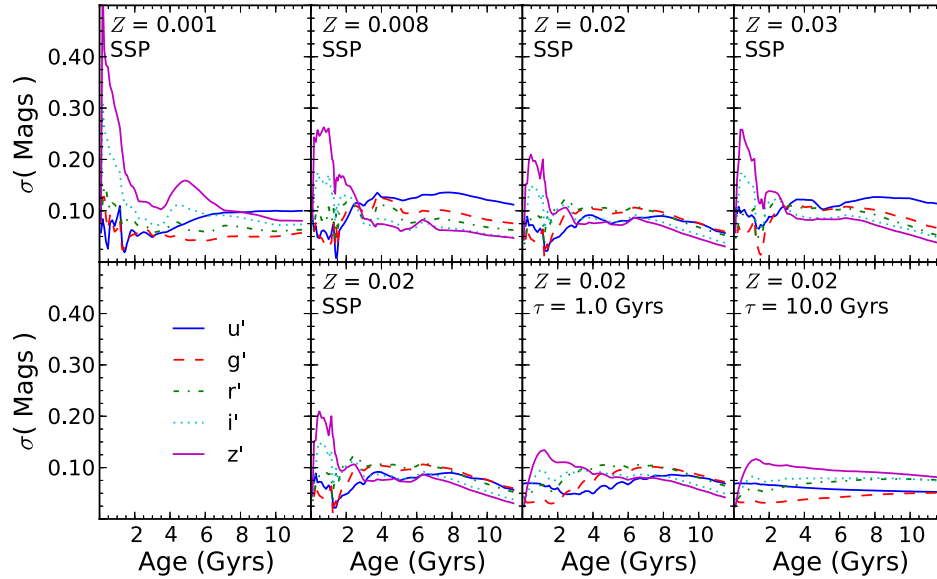


FIG. 2.—Scatter between the predicted magnitudes of the models for the Sloan filters as a function of age. In all panels the standard deviation between the magnitude predictions of four model sets (BC03; M05; CB07; C09) through each filter is plotted vs. age. In the top series of panels, all the models are for an SSP with a Salpeter IMF and various metallicities. *Bottom*: The figure legend is shown at the far left. The remaining plots show stellar populations with a Salpeter IMF, solar metallicity, and star-formation histories that vary from shorter to longer timescales going left to right. See the electronic edition of the *PASP* for a color version of this figure

a Salpeter IMF. The left panel in Figure 4 is for models with solar metallicity, and the right panel is for models with a metallicity of $Z = 0.001$. Each panel is divided into four plots, corresponding to four different ages: 1 Gyr (*top left*), 2 Gyr (*top right*), 6 Gyr (*bottom left*), and 10 Gyr (*bottom right*). The lines in each plot represent the differences between the predicted absolute magnitude through each filter in each model set (BC03;

M05; CB07; C09) minus the predicted absolute magnitude of BC03. In general, the models are distributed throughout the full range of magnitudes covered by the models. This shows that apparent disagreements in Figures 2 and 3 are not caused by one discrepant model set. Therefore, the scatter seen in Figures 2 and 3 is representative of the general uncertainties between the SPS models.

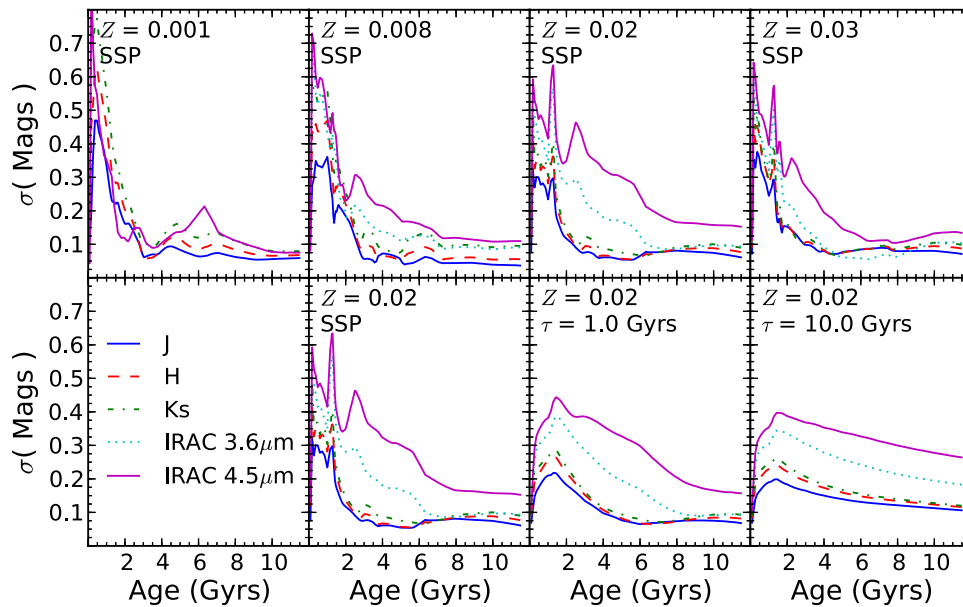


FIG. 3.—Same as Fig. 2, but for 2MASS J , H , and K_s and *Spitzer*/IRAC 3.6 and 4.5 μm . See the electronic edition of the *PASP* for a color version of this figure

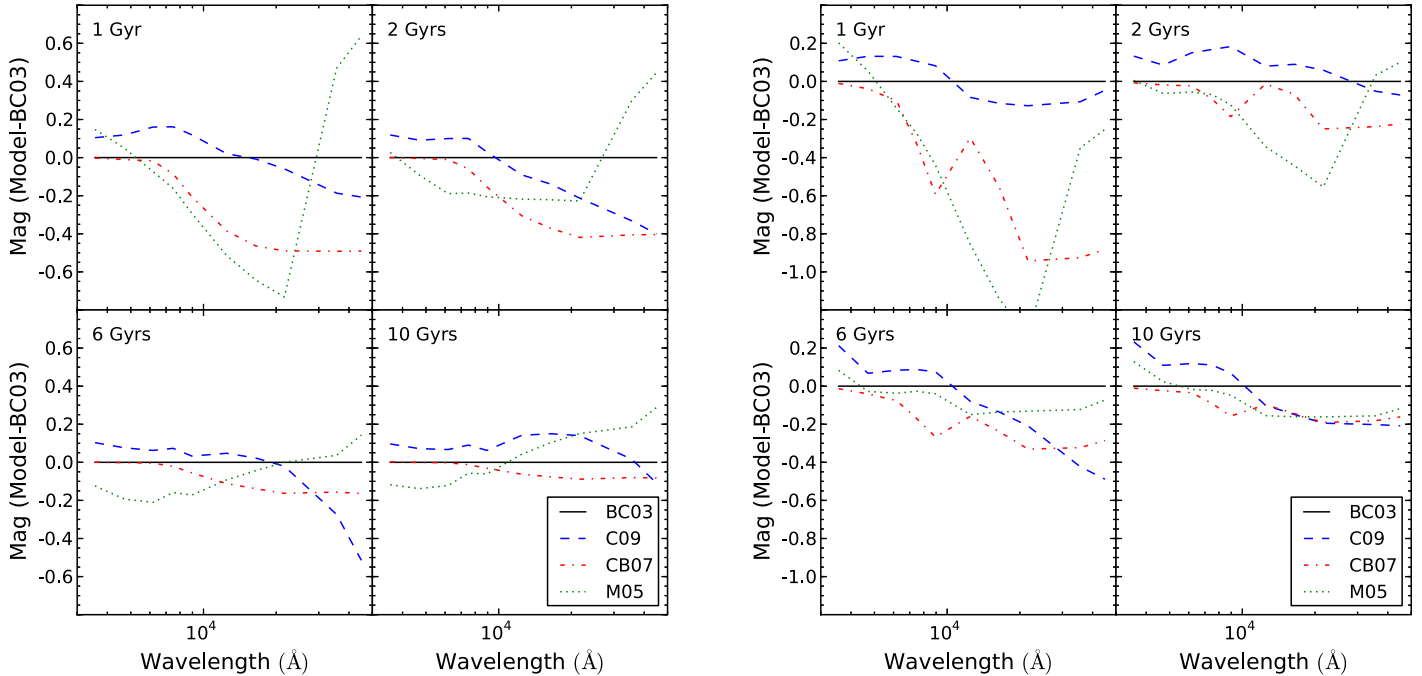


FIG. 4.—Differences between models for solar (*left*, $Z = 0.02$) and subsolar (*right*, $Z = 0.001$) metallicities. Models are for an SSP with a Salpeter IMF. Lines represent the difference between the predicted rest-frame absolute magnitudes minus the predictions of the BC03 model set as a function of filter wavelength. Each panel is divided up into four different plots representing the differences between model predictions at four different ages. See the electronic edition of the *PASP* for a color version of this figure

Finally, we note that our results are robust against the choice of model sets used for our comparison. For instance, it might seem expedient to exclude the BC03 models from the above analysis, because substantial effort has been put forth to understand the TP-AGB phase since BC03 was published. However, excluding this model set from the analysis makes no appreciable differences in our results, which simply reflects the fact that the BC03 models are rarely an outlier in Figure 4. Our conclusions also remain unchanged if we instead compare the P09, M05, and C09 model sets with a Kroupa IMF. This once again emphasizes that the differences noted in this article reflect general uncertainties in SPS modeling and are not caused by one discrepant model set.

3.4. A Practical Example

We perform one final model comparison to demonstrate the utility of EzGal, as well as to reinforce the above results and show how they can impact current work. We generate new CSP models for our model sets using a more physically motivated star-formation history (SFH), which is the global SFH of the universe. We use the global star-formation-rate density as a function of redshift from González et al. (2010), which includes data from Reddy & Steidel (2009), Bouwens et al. (2008), Bouwens et al. (2007), and Schiminovich et al. (2005). This gives the relative star-formation rate in the universe as a func-

tion of redshift from $z = 0.3$ to $z = 8.5$. We further set the star-formation rate to zero at $z = 0$ and $z > 10$ to prevent our star-formation history from having any discontinuities. While the star-formation rate is unlikely to turn on suddenly at $z = 10$ or to turn off at $z = 0$, in practice, this assumption makes little difference and does not impact our example.

Using EzGal we generate a CSP from this star-formation history for a solar-metallicity galaxy with a Salpeter IMF for our four comparison models (BC03; M05; CB07; C09). We then use EzGal to generate apparent magnitude predictions for each CSP model through the Sloan r , 2MASS H , and IRAC $3.6 \mu\text{m}$ filters as a function of redshift, assuming a formation redshift of $z_f = 10.0$. Finally, we calculate the scatter between the predicted magnitudes of the models in the same way as in our previous comparisons. We show the scatter between models as a function of filter and redshift in Figure 5, as well as the star-formation history used to generate the CSP models.

The trends seen in Figure 5 are caused primarily by two effects: increasing model uncertainty for younger stellar populations and the changing rest-frame wavelengths traced by each filter as a function of redshift. For $3.6 \mu\text{m}$ the model scatter peaks in the $1 \lesssim z \lesssim 3$ range. At higher redshifts the $3.6 \mu\text{m}$ filter traces the rest-frame optical, where the models agree well. Strong star formation from $2 \lesssim z \lesssim 5$ guarantees that there is a substantial presence of young stars over this redshift range; therefore, the increasing importance of TP-AGB stars leads

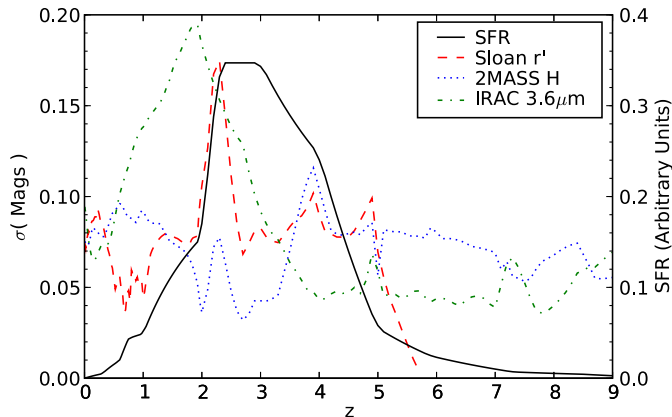


Fig. 5.—Scatter between models as a function of redshift for BC03, M05, CB07, and C09 models with solar metallicity, a Salpeter IMF, and with a SFH given by the global star-formation history of the universe. The global SFH used comes from González et al. (2010). Scatter refers to the standard deviation of the predicted magnitudes from all four bands at a given redshift and for a given filter. The scatter in Sloan r cuts off at $z \sim 6$, where it is tracing rest-frame wavelengths blueward of the Lyman limit and is therefore unobservable. See the electronic edition of the *PASP* for a color version of this figure

to increased uncertainty, as does the fact that the $3.6 \mu\text{m}$ filter traces longer wavelengths, where TP-AGB stars are again more important. For $z \lesssim 2$ the star-formation rate begins to drop and the stellar populations become steadily older. Since the models agree well for old ages, this causes the model scatter to peak shortly after the star-formation rate peaks and then steadily decline to $z = 0$.

In the H band the scatter between models is relatively constant and typically $\lesssim 0.1$ mag. This low scatter occurs because the H -band filter always traces regions of parameter space for which the models agree well. At high redshift, when the stellar populations are young and the impact of TP-AGB stars is important, the H band traces the rest-frame optical, which is unaffected by TP-AGB stars. At low redshift the steadily dropping star-formation rate leads to an increasing mean age, once again minimizing the impact of TP-AGB stars and leading to low uncertainties.

Similarly, for Sloan r , the scatter between models is typically $\lesssim 0.1$ mag at low and high redshifts. However, there is a strong and sudden peak in the model scatter at $z \sim 2$. This same feature is also present at precisely the same redshift and significance in all the Sloan filters and the J band, although we only show Sloan r in Figure 5. The fact that this peak shows up in a variety of filters at the same redshift means that the underlying uncertainty depends primarily on age, not wavelength. At this redshift, the Sloan filters and the J band are all tracing rest-frame wavelengths blueward of the 4000 \AA break. In contrast, both the H band and IRAC $3.6 \mu\text{m}$ filters trace wavelengths redward of the 4000 \AA break, and neither has evidence for a similar increase in model scatter. Therefore, we conclude that

this peak in model scatter is caused by uncertainty in modeling young stellar populations blueward of the 4000 \AA break.

Most importantly, Figure 5 illustrates one more reason that it is important to use quantitative methods to estimate the impact of SPS model uncertainties. Observations of galaxies at various redshifts through a given filter will trace stellar populations with a variety of ages and wavelengths. Moreover, the uncertainties in SPS modeling depend sensitively on wavelength and age. The result of these facts is that, in practice, SPS model uncertainty often depends on redshift in ways that are difficult to predict. Therefore, for studies that investigate how stellar populations evolve as a function of redshift, it is vital to verify that this redshift-dependent model uncertainty is not causing spurious results. This is best done through quantitative comparison of the models with each other or of the observations with many different models—tasks for which EzGal is designed.

4. EZGAL WEB RESOURCES

A number of EzGal resources are available through the EzGal Web page,⁵ including two different interfaces. The first interface⁶ allows the user to instantly download magnitude, k -correction, e -correction, $e + k$ -correction, mass-to-light ratio, mass, and solar magnitudes for a given model set and filter as a function of redshift for a set of precalculated formation redshifts and cosmologies. The second interface⁷ allows for arbitrary choice of formation redshift and cosmology and e-mails the calculated results to the user, which typically takes a minute or two.

An up-to-date copy of Table 2 is maintained on the EzGal Web page with basic filter information, solar magnitudes, and calculated AB-to-Vega conversions listed for all filters available through the Web page. Also distributed with this table is a plot of magnitude, mass-to-light ratio, and k -correction evolution as a function of redshift for each filter, a plot of the filter response curve, and a data file giving the filter response curve used by EzGal.

A download page is provided where the source code for EzGal can be downloaded, as well as EzGal-ready model files. This includes the original SSP models distributed with all the model sets discussed in this article, as well as the interpolated SSPs and generated CSPs that we use for our comparison. Finally, we distribute a manual for the EzGal API (application programming interface) that describes how to use EzGal from within Python.

5. CONCLUSIONS

EzGal provides a convenient framework for transforming SPS models from theoretical quantities to directly observable magnitudes and colors. It includes code for generating

⁵ See <http://www.baryons.org/ezgal/>.

⁶ See <http://www.baryons.org/ezgal/model>.

⁷ See http://www.baryons.org/ezgal/model_server.

composite stellar population models with arbitrary star-formation histories and dust extinction. In principle, it can work with any model set, providing a simple and consistent framework for comparing the predictions of different model sets and estimating errors introduced by the choice of model set.

We demonstrate the latter property of EzGal by predicting the magnitude evolution for five model sets (BC03; M05; CB07; C09; P09) as a function of age, filter, metallicity, and star-formation history. We compare the predictions between the models and note substantial uncertainty (0.3–0.7 mag) for young stellar populations (ages $\lesssim 2$ Gyr) at long wavelengths ($\lambda \gtrsim 1 \mu\text{m}$): a region of well-known uncertainty caused by the contribution of thermally pulsating AGB stars. We note that for old ages, optical filters, and solar metallicities, the models agree at the ~ 0.1 mag level. For subsolar-metallicity models with old ages and at all wavelengths, the models agree as well as, if not better than, subsolar metallicities. This likely reflects the fact that the models are all compared with (or calibrated with) Milky Way globular clusters. These differences are best viewed as lower limits on the uncertainties inherent in SPS modeling, because it does not include systematic errors in assumptions or methodologies that are shared by all model sets.

Finally, we calculate the scatter between our models for a solar-metallicity stellar population with a Salpeter IMF and a star-formation history matching the global star-formation history of the universe. We conclude that the derived model uncertainty depends upon redshift and filter in ways that are difficult to predict. This highlights the importance of using quantitative

methods to estimate model uncertainty, especially when comparing observations with models as a function of redshift.

These results illustrate the utility of EzGal in simplifying the process of working with SPS model sets, making it easy to compare observations with multiple model sets, as well as to compare model sets with each other. In turn, this provides a simple method to quantify the uncertainties introduced by the choice of SPS model set, as well as to find robust or disparate regions in parameter space (age, wavelength, metallicity, etc.). We hope this will help other researchers with both interpreting data and planning new observations. We emphasize that the model sets used throughout this article are not our own work, but are the work of a number of different groups and individuals. As such, understanding the models and the differences between them is best accomplished by referring to the original articles.

We gratefully acknowledge the authors of all five of the model sets included in this article for giving us permission to redistribute their work in this way. We especially thank Charlie Conroy, Maurizio Salaris, Santi Cassisi, Stéfané Charlot, Gustavo Bruzual, and Claudia Maraston for their input on this project. We are also grateful to our many collaborators—Adam Stanford, Peter Eisenhardt, Yen-Ting Lin, Greg Snyder, and others—who have tested EzGal extensively and provided us with invaluable feedback. Finally, we would like to thank the anonymous referee whose comments have greatly improved the presentation in this article. This article is based upon work supported by the National Science Foundation under grant AST-0708490.

REFERENCES

- Blanton, M. R., & Roweis, S. 2007, *AJ*, 133, 734
 Bohlin, R. C., & Gilliland, R. L. 2004, *AJ*, 127, 3508
 Bouwens, R. J., Illingworth, G. D., Franx, M., & Ford, H. 2007, *ApJ*, 670, 928
 ———. 2008, *ApJ*, 686, 230
 Bruzual, G., & Charlot, S. 2003, *MNRAS*, 344, 1000, BC03
 Cappellari, M., McDermid, R. M., Alatalo, K., Blitz, L., Bois, M., Bournaud, F., Bureau, M., Crocker, A. F., et al. 2012, *Nature*, 484, 485C
 Charlot, S., & Fall, S. M. 2000, *ApJ*, 539, 718
 Colina, L., Bohlin, R. C., & Castelli, F. 1996, *AJ*, 112, 307
 Conroy, C., & Gunn, J. E. 2010, *ApJ*, 712, 833
 Conroy, C., Gunn, J. E., & White, M. 2009, *ApJ*, 699, 486, C09
 Fotopoulou, S., Salvato, M., Hasinger, G., Rovilos, E., Brusa, M., Egami, E., Lutz, D., Burwitz, V., et al. 2012, *ApJS*, 198, 1
 González, V., Labbé, I., Bouwens, R. J., Illingworth, G., Franx, M., Kriek, M., & Brammer, G. B. 2010, *ApJ*, 713, 115
 Jonsson, P. 2006, *MNRAS*, 372, 2
 Komatsu, E., Smith, K. M., Dunkley, J., Bennett, C. L., Gold, B., Hinshaw, G., Jarosik, N., Larson, D., et al. 2011, *ApJS*, 192, 18
 Kriek, M., van Dokkum, P. G., Whitaker, K. E., Labbé, I., Franx, M., & Brammer, G. B. 2011, *ApJ*, 743, 168
 Ma, J., Wang, S., Wu, Z., Fan, Z., Zhang, T., Wu, J., Zhou, X., Jiang, Z., et al. 2012, *AJ*, 143, 29
 Mancone, C. L., Gonzalez, A. H., Brodwin, M., Stanford, S. A., Eisenhardt, P. R. M., Stern, D., & Jones, C. 2010, *ApJ*, 720, 284
 Maraston, C. 2005, *MNRAS*, 362, 799, M05
 Marigo, P., Girardi, L., Bressan, A., Groenewegen, M. A. T., Silva, L., & Granato, G. L. 2008, *A&A*, 482, 883
 Marín-Franch, A., Aparicio, A., Piotto, G., Rosenberg, A., Chaboyer, B., Sarajedini, A., Siegel, M., Anderson, J., et al. 2009, *ApJ*, 694, 1498
 Percival, S. M., Salaris, M., Cassisi, S., & Pietrinferni, A. 2009, *ApJ*, 690, 427
 Reddy, N. A., & Steidel, C. C. 2009, *ApJ*, 692, 778
 Schiminovich, D., Ilbert, O., Arnouts, S., Milliard, B., Tresse, L., Le Fèvre, O., Treyer, M., Wyder, T. K., et al. 2005, *ApJ*, 619, L 47
 Taylor, E. N., Hopkins, A. M., Baldry, I. K., Brown, M. J. I., Driver, S. P., Kelvin, L. S., Hill, D. T., Robotham, A. S. G., et al. 2011, *MNRAS*, 418, 1587